Annals of Biomedical Engineering, Vol. 41, No. 4, April 2013 (© 2012) pp. 694–708
DOI: 10.1007/s10439-012-0712-3

A Pull-Back Algorithm to Determine the Unloaded Vascular Geometry in Anisotropic Hyperelastic AAA Passive Mechanics

FABIÁN RIVEROS,[1] SANTANU CHANDRA,[3] ENDER A. FINOL,[4] T. CHRISTIAN GASSER,[5] and JOSE F. RODRIGUEZ[1,2]

[1]Mechanical Engineering Department/Aragon Institute of Engineering Research, Universidad de Zaragoza, Zaragoza, Spain; [2]Biomedical Research Networking Center in Bioengineering, Biomaterials and Nanomedicine (CIBER-BBN), Zaragoza, Spain; [3]Department of Aerospace and Mechanical Engineering, University of Notre Dame, Notre Dame, IN, USA; [4]Department of Biomedical Engineering, The University of Texas at San Antonio, San Antonio, TX, USA; and [5]Department of Solid Mechanics, School of Engineering Sciences, The Royal Institute of Technology (KTH), Osquars Backe 1, 100 44 Stockholm, Sweden

(*Received 26 July 2012; accepted 20 November 2012; published online 29 November 2012*)

Associate Editor Joan Greve oversaw the review of this article.

Abstract—Biomechanical studies on abdominal aortic aneurysms (AAA) seek to provide for better decision criteria to undergo surgical intervention for AAA repair. More accurate results can be obtained by using appropriate material models for the tissues along with accurate geometric models and more realistic boundary conditions for the lesion. However, patient-specific AAA models are generated from gated medical images in which the artery is under pressure. Therefore, identification of the AAA zero pressure geometry would allow for a more realistic estimate of the aneurysmal wall mechanics. This study proposes a novel iterative algorithm to find the zero pressure geometry of patient-specific AAA models. The methodology allows considering the anisotropic hyperelastic behavior of the aortic wall, its thickness and accounts for the presence of the intraluminal thrombus. Results on 12 patient-specific AAA geometric models indicate that the procedure is computational tractable and efficient, and preserves the global volume of the model. In addition, a comparison of the peak wall stress computed with the zero pressure and CT-based geometries during systole indicates that computations using CT-based geometric models underestimate the peak wall stress by 59 ± 64 and 47 ± 64 kPa for the isotropic and anisotropic material models of the arterial wall, respectively.

Keywords—Abdominal aortic aneurysm (AAA), Patient-specific, Image-based, Zero pressure geometry, FEA, Anisotropy.

INTRODUCTION

An abdominal aortic aneurysm (AAA) is an abnormal widening of the aorta, commonly developed below the renal arteries and above the iliac bifurcations. The natural course of aneurysm disease is a progressive aortic enlargement combined with weakening of the wall tissue that may result in aortic rupture.[35]

The prevalence of AAA is 8.8% in the population above the age of 65, accounting for more than 15,000 deaths in the US and 8,000 in the United Kingdom every year.[27] The indications for aneurysm repair (either surgical or endovascular) are largely based upon the presence of symptoms, aneurysm size, and the rate of expansion. Patients with symptomatic aneurysms should undergo repair, regardless of aneurysm diameter. Patients with asymptomatic aneurysms that reach a diameter of 5.5 cm should be considered for repair.[28] Early repair may be beneficial in patients whose aneurysm increases ≥0.5 cm in diameter in 6 months.[20,23]

Although the criterion for AAA repair varies in practice, the maximum diameter is the most frequently used clinical AAA repair indication. However, the diameter criterion is under controversial discussion since only 25% of AAAs rupture in a patient's lifetime.[3] Consequently, small AAAs (<5.5 cm) rupture and large AAAs (>5.5 cm) remain stable, whereas surgical interventions continue to pose serious risk especially in elder patients.[41] Therefore, alternative rupture risk indices have been proposed in order to target patients that require AAA repair. Specifically, biomechanical parameters like peak wall stress (PWS)

Address correspondence to Jose F. Rodriguez, Mechanical Engineering Department/Aragon Institute of Engineering Research, Universidad de Zaragoza, Zaragoza, Spain. Electronic mail: jfrodrig@unizar.es

or peak wall rupture risk (PWRR) have shown to be a feasible an promising alternative that can be used to better ascertain the risk of rupture.[10,11,13,18,25,31,42–46] The computation of such parameters requests (i) accurate methods for reliable reconstruction of the aortic geometry, (ii) appropriate material properties for the aneurysmatic tissues, and (iii) realistic (physiological) boundary conditions, and (iv) along with adequate numerical methods must be developed to solve the biomechanical problem.[12]

Planar biaxial testing by Vande Geest *et al.*[44] demonstrated that the aneurysmal degeneration of aortic tissue leads to an increase in mechanical anisotropy, with the circumferential direction being stiffer. This study also showed that the aneurysm wall of the average population is highly nonlinear but rather isotropic. This motivated the development of improved constitutive models for the AAA wall[34,44] permitting more elaborated computations of AAA and the reassessment of established biomechanical markers of AAA rupture risk.[32–34]

The reconstructed AAA geometry from CT images is pressurized, and hence, it is not the zero-pressure configuration. Specifically, for most CT modalities, the geometry seen in the images refers to the configuration that is inflated with the diastolic blood pressure. Assuming this geometry being the zero-pressure configuration, as it has been done frequently, naturally generates incorrect deformations and stresses relative to the *in vivo* condition. Consequently, recent studies[6,24,29,40] introduced a hypothetical zero-pressure configuration, which in turn serves as the reference for biomechanical simulations. Specifically, a more realistic computation of the PWS should consider such a zero-pressure geometry. When loading the zero-pressure configuration with the diastolic blood pressure, the deformed AAA is thought to match the AAA geometry seen in the CT images. This constraint implicitly defines the shape of the zero-pressure configuration, and a number of alternatives have been presented to solve this problem.[6,24,29] One approach relies on inverse elastostatic methods. These methods were first introduced by Shield[36] for elastically homogeneous materials and zero body forces and later generalized for elastic materials of any grade by Carlson.[4] Later, Chadwick[5] exploited the duality property demonstrated by Shield to formulate Shield's equilibrium equations in terms of Eshelby's energy–momentum tensor. These results were further re-examined by Govindjee and Mihalic[15,16] in order to provide a more suitable finite element formulation. This formulation involved minor changes to elements designed for traditional finite element analysis, and could be applied to nearly incompressible materials. The formulation proposed by Govindjee and Mihalic was applied by Lu *et al.*[24] to find the zero-pressure configuration of AAAs. It is noted that the inverse method requires manipulations on the finite element matrices, which makes its application difficult when using commercial finite element solvers. However, many of the reported approaches to compute the zero-pressure configuration considered shell models of the AAA geometry,[24,29] and all of them investigated only isotropic aneurysm wall models. Most severely, none of the reported studies accounted for an intraluminal thrombus (ILT) when predicting the zero-pressure configuration. An ILT is seen in almost all clinical relevant AAAs.[21]

The present work presents an algorithm to determine the zero-pressure geometry of an AAA and overcomes the above mentioned limitations. Specifically, the proposed methodology accounts for the wall's anisotropy and the presence of the ILT. The algorithm is a modification of the method proposed by Raghavan *et al.*,[29] which continuously updates the zero pressure geometry based on the displacement field rather than on an incremental upgrading of the deformation gradient, as proposed by de Putter *et al.*[6] The proposed approach offers some numerical advantages with respect to the methodology proposed by de Putter *et al.* Most important, our computations always start from an updated reference configuration, instead from an initially deformed configuration, such that the proposed methodology avoids using small increments at the initial steps. This leads to numerical efficiency through fast convergence. The proposed method has been implemented on commercial finite element analysis software ABAQUS (ver 6.9, Hibbitt, Karlson and Sorensen, Inc., Pawtucker, RI) using solid meshes for both the AAA wall and the ILT. The efficacy of the procedure is demonstrated by one idealized and 12 patient-specific AAA geometries.

METHODS

Image Acquisition and 3D Reconstruction

Twelve non-ruptured patient-specific AAA geometries have been developed for this study. Two of these models, named A1 and A2, were obtained from medical images at Allegheny General Hospital (Pittsburgh, PA) from asymptomatic subjects who were eligible for elective endovascular repair. The term non-ruptured is used in the context that all CT images were acquired following a standard imaging protocol before the subjects underwent repair or during the surveillance period after diagnosed with AAA. The 3D computational models were developed through image processing and segmentation of the available CT image slices (resolution of 512×512, average pixel size of 0.769 mm and average slice thickness of 3 mm). The

DICOM formatted CT images were imported in the ScanIP module of Simpleware™ (Exeter, UK) for segmentation. A semi-automatic methodology[26,37–39] was followed to segment and create the masks for the three domains (i.e., lumen, ILT, and AAA wall). Ten additional non-ruptured AAA geometries, named B1–B10, were acquired at two hospitals in Stockholm, Sweden. All AAA images provided a sufficiently high out-of-plane resolution of the image data and a good identification of the exterior aneurysm surface. Local ethics committee approved the collection and use of anonymized data from human. Aneurysms B1–B10 were reconstructed with the diagnostic software A4research (VASCOPS GmbH, Graz, Austria), which was applied by an operator with engineering background assisted by a radiologist to ensure proper segmentation of the aneurysms. Details regarding the image segmentation process are given elsewhere.[2] All reconstructed models include the ILT and assumed a non-homogeneous aneurysm wall thickness varying between 1.5 and 1.13 mm at the thrombus-free and covered sites respectively.[22]

All surface geometries were exported in STereo Lithography (STL) file format and meshed with the ANSYS-ICEM software (ANSYS, Inc., Canonsburg, PA). The resulting 3D models were then subject to finite element analysis with the software ABAQUS following the proposed iterative algorithm to obtain the zero pressure geometry.

Material Models

We consider the material of the aneurysm wall and ILT as hyperelastic. For the wall, isotropic and anisotropic constitutive equations were used, where as for the ILT, isotropic behavior has been assumed. We postulate the existence of a strain-energy function (SEF) W from which the stress–strain behavior of the material can be derived. To express W as a function of the invariants we employ the multiplicative decomposition for the deformation gradient $F = F_{\text{vol}}\overline{F}$ into a volumetric part $F_{\text{vol}} = J^{+1/3}\text{I}$ and an isochoric part $\overline{F} = J^{-1/3}F$, with the volume ratio $J = \det F > 0$ and $\det \overline{F} = 1$. Under these considerations the SEF W can be written as

$$W(C, a_0) = U(J) + \overline{W}(\overline{I}_1, \overline{I}_2, \overline{I}_4), \tag{1}$$

where $C = F^{\text{T}}F$ is the right Cauchy-Green tensor and $\mathbf{a}_0$ denotes a unit vector along the direction of anisotropy of the tissue which is assumed to coincide with the circumferential direction of the vessel. The volumetric elastic response U and isochoric elastic response $\overline{W}$ of the material are given scalar-valued functions of J and the invariants $\overline{I}_1, \overline{I}_2, \overline{I}_4$, which are expressed in terms of $\overline{C} = \overline{F}^{\text{T}}\overline{F}$, the modified right Cauchy-Green tensor, and $\mathbf{a}_0$ as

$$\begin{aligned} &\overline{I}_1 = tr\overline{C}, \quad \overline{I}_2 = \frac{1}{2}\left[\left(tr\overline{C}\right)^2 - tr\overline{C}^2\right], \\ &\overline{I}_4 = a_0 \cdot \overline{C} \cdot a_0. \end{aligned} \tag{2}$$

The second Piola-Kirchoff stress tensor can be obtained from the defined SEF as[19]:

$$S = JpC^{-1} + 2J^{-2/3}\sum_{\substack{i=1 \\ i\neq 3}}^{4} \frac{\partial \overline{W}}{\partial \overline{I}_i}\text{DEV}\left(\frac{\partial \overline{I}_i}{\partial \overline{C}}\right) \tag{3}$$

where $p = dU/dJ$ is the constitutive equation for the hydrostatic pressure p, and $\text{DEV}(\cdot) = (\cdot) - \frac{1}{3}[(\cdot) : C]C^{-1}$ is the deviatoric operator in the Lagrangian description. The Cauchy stress tensor can be derived from the previous definition as

$$\sigma = J^{-1}FSF^{\text{T}} \tag{4}$$

For the case of isotropy, the material response of the aneurysm wall tissue was characterized by the SEF[7]:

$$W_{\text{wall}}^{\text{iso}} = \kappa(J-1)^2 + D_1\left(e^{D_2(\overline{I}_1 - 3)} - 1\right) \tag{5}$$

where D_1 and D_2 are material parameters and κ is the volumetric modulus.

For the case of anisotropy, the aneurysmal wall tissue was modeled by a SEF[34]:

$$\begin{aligned} W_{\text{wall}}^{\text{aniso}} = &\kappa(J-1)^2 + D_1\left(e^{D_2(\overline{I}_1 - 3)} - 1\right) \\ &+ \frac{k_1}{k_2}\left(e^{\kappa_2(\overline{I}_4 - 1)^2}\right) - 1 \end{aligned} \tag{6}$$

where D_1, D_2, k_1, k_2 are material parameters. This approach was used due to the lack of histologic evidence regarding the fiber distribution in aneurysmal tissue. The wall's stiffer response corresponds to its circumferential direction, i.e., as it has been verified through biaxial testing in Vande Geest *et al.*[44]

The material parameters for the constitutive models, Eqs. (5) and (6), were obtained by means of a nonlinear regression analysis of the mean biaxial test for aneurysmal tissue reported in Vande Geest *et al.*[44] Table 1 shows the identified model parameters for both constitutive models. Figure 1 shows the fit for the isotropic model, Eq. (5), to the original data reported by Vande Geest ($R^2 = 0.943$), where as Fig. 2 shows the same results for the anisotropic model ($R^2 = 0.953$). Both models produce comparable results since the mean stress–strain data reported in Vande Geest *et al.*[44] shows little degree of anisotropy. We also note that, even though our material model takes into account the behavior of aneurysmal tissue, either model (Eqs. (5)

TABLE 1. Material parameters for the isotropic, Eq. (5), and anisotropic, Eq. (6), aneurysmal wall tissue constitutive models.

Model	D_1 (kPa)	D_2	κ (kPa)	k_1 (kPa)	k_2
Isotropic	0.214	41.3	10^4	–	–
Anisotropic	0.214	41.3	10^4	0.212	130

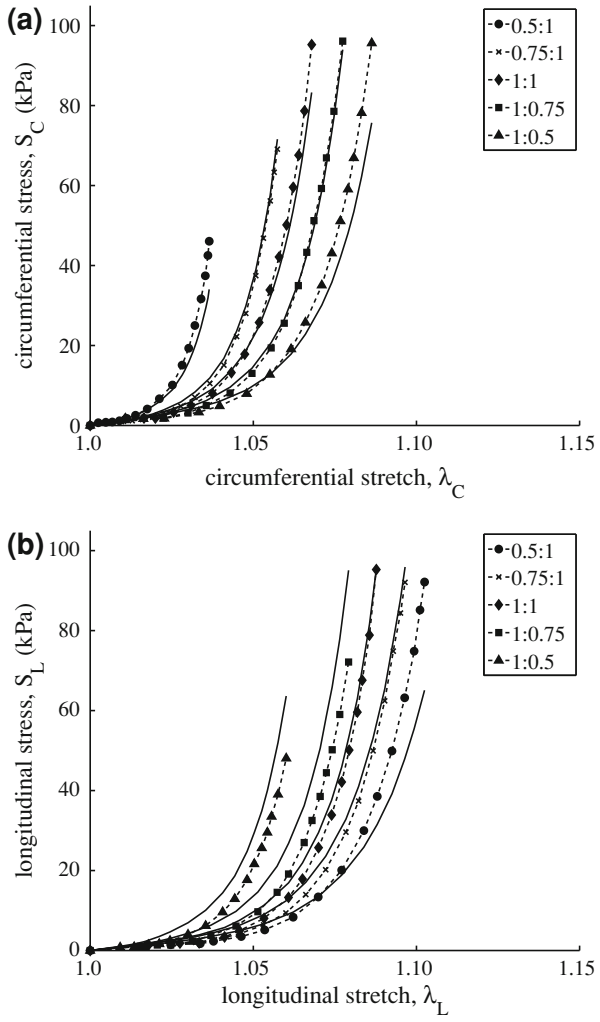

FIGURE 1. Biaxial experimental data from Vande Geest *et al.*[44] vs. predicted results by the isotropic SEF Eq. (5) in the (a) circumferential and (b) longitudinal directions.

and (6)) does not distinguish between distinct wall layers. While the healthy arterial wall is made of intima, medial and adventitia layers, this normal structure is lost at the onset of aneurysmal disease.[14]

The ILT has been modeled as an isotropic hyperelastic material with the SEF proposed by Di Martino and Vorp[8]:

$$W_T = C_{20}(\bar{I}_2 - 3) + C_{02}(\bar{I}_2 - 3)^2, \qquad (7)$$

where C_{20} and C_{02} are material constants with dimensions of stress and $\bar{I}_2$ the second modified invariant. The reported parameters used were $C_{20} = 28$ kPa and $C_{02} = 28.6$ kPa.

Finite Element Models

The proposed algorithm was validated using an idealized model of a thick wall cylinder subject to internal pressure. In addition, the algorithm was applied to 12 three-dimensional AAA patient-specific geometries. Table 2 summarizes the geometric characteristics and mesh sizes used for each of the 12 AAA geometries. Each geometry was discretized with linear tetrahedrons and nearly isotropic meshes. The total number of elements per AAA model ranged between 430,000 and 635,000 elements, and had at least three elements across the arterial wall thickness in order to capture the stress gradients in the wall. Figure 3 shows the finite element meshes for models A1 and A2.

The isotropic and anisotropic material models for the arterial wall were implemented in the material user subroutines UHYPER (for the isotropic material model) and UANISOHYPER_INV (for the anisotropic material model) within the finite element software ABAQUS. The constraints due to the thoracic aorta and common iliac arteries were simulated by restraining the longitudinal displacement while allowing displacements in the radial direction.

The assessment of the direction of anisotropy has been performed following the procedure proposed by Alastrue *et al.*[1] In this procedure, the model is subjected to a sub-diastolic pressure using the isotropic material model described by Eq. (5). Then, the direction of anisotropy is made coincident with the direction of maximum principal stress. The result obtained when this procedure is applied is a dominant circumferential direction of the fibers shown in Fig. 4 for models A1 and A2. Note that the aneurysmal model considers uniform mechanical properties, and we made no distinction between the aneurysm and the adjacent vasculature. A refined model should consider the variation in the mechanical properties between the arterial and aneurysmal tissues since otherwise stress concentrations would appear at the interfaces.

Internal pressures of 10.6 kPa (80 mmHg) and 16 kPa (120 mmHg) were applied to the lumen surface to simulate the diastolic and systolic pressures, respectively. The diastolic pressure was used during the iterative algorithm to find the unloaded configuration, as this was considered the intraluminal pressure when the images were acquired. The systolic pressure was used to find the largest stresses on the AAA.

To test the quality of the mesh used for the calculations, a sensitivity analysis was performed on model A2 subject to diastolic pressure. Table 3 shows the peak principal stress (PWS) in the AAA wall for

different mesh densities. As these results demonstrate, for meshes of more than 300,000 elements, the maximum principal stress changes less than a 3% with respect to the finest mesh used, while giving a sufficient number of elements through the arterial wall as shown in Fig. 3a (a minimum of three elements at any section of the model). Details regarding the ILT and arterial wall mesh for all models are given on Table 2.

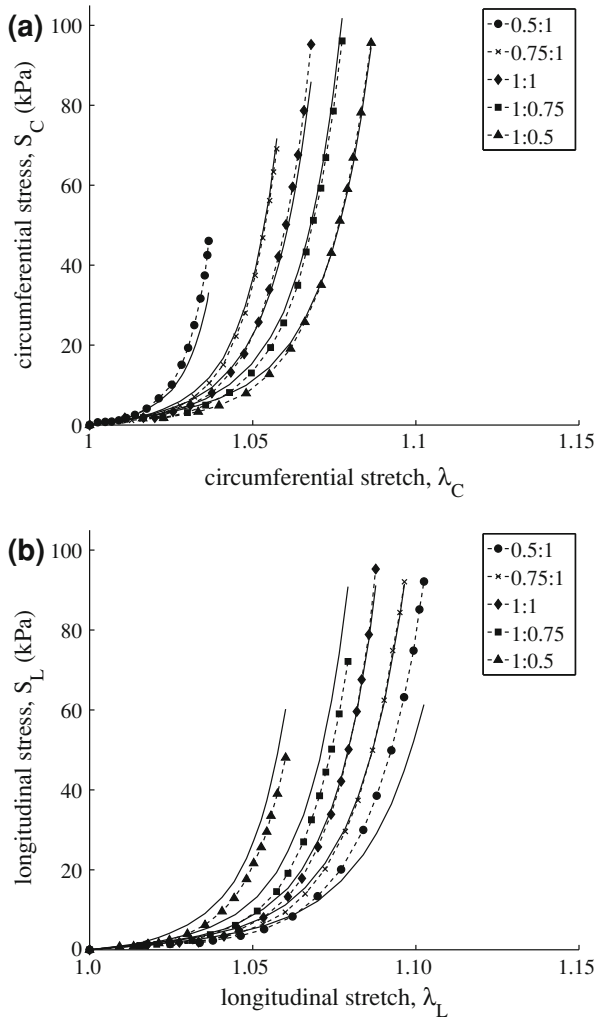

FIGURE 2. Biaxial experimental data from Vande Geest *et al.*[44] vs. predicted results by the anisotropic SEF Eq. (6) in the (a) circumferential and (b) longitudinal directions.

Zero-Pressure Geometry Algorithm

The algorithm to reconstruct the zero-pressure geometry of an AAA model from the CT image based geometry is explained in the following. The main purpose of this algorithm is to find the zero-pressure configuration, i.e., a reference configuration that deforms into the geometry X_{image} that is seen in the CT images when subjected to the diastolic pressure, P_{diast}. The proposed algorithm keeps the mesh connectivity unchanged and iteratively updates the nodal coordinates. When working with the anisotropic material, the local circumferential direction is also consistently pulled-back to the zero-pressure configuration.

The iterative algorithm is outlined in Fig. 5, where B denotes a configuration of the AAA. The initial zero-pressure configuration B_0 corresponds to the geometry that was reconstructed from the CT image, X_{image}, where X represents a $N_n \times 3$ matrix that stores the nodal coordinates of the finite element mesh. Here, N_n denotes the total number of mesh nodes, and for an anisotropic material model ($f_{\text{aniso}} = 1$) the circumferential direction is also provided at the element level. Now iterative algorithm starts and of the zero-pressure configuration is updated until the error norm, i.e., the absolute maximum nodal distance between X_{image} and the deformed configuration from inflating the current zero-pressure configuration, X_{def}, is less than a prescribed tolerance *tol*.

Step i At the kth iteration an elastic problem is solved that considers the $k-1$th zero-pressure geometry as its stress-free reference configuration. Constitutive relations and boundary conditions apply as described in the previous section.

TABLE 2. Characteristics of the 12 patient-specific AAA models.

Model	Max diameter (cm)	Max ILT thickness (cm)	Arterial wall elements	ILT elements	Total elements
A1	5.1	1.1	322,228	110,985	433,213
A2	5.0	1.8	247,850	198,876	446,726
B1	5.1	2.0	354,865	181,423	536,288
B2	4.2	1.1	336,766	242,191	578,957
B3	5.1	1.4	285,509	291,834	577,343
B4	5.0	2.1	287,576	199,300	486,876
B5	5.4	0.9	346,193	288,170	634,363
B6	5.1	2.4	308,788	239,911	548,699
B7	4.4	0.2	368,482	243,630	612,112
B8	4.8	2.1	338,181	213,913	552,094
B9	5.1	2.1	333,169	279,490	612,659
B10	4.7	1.0	292,151	282,051	574,202

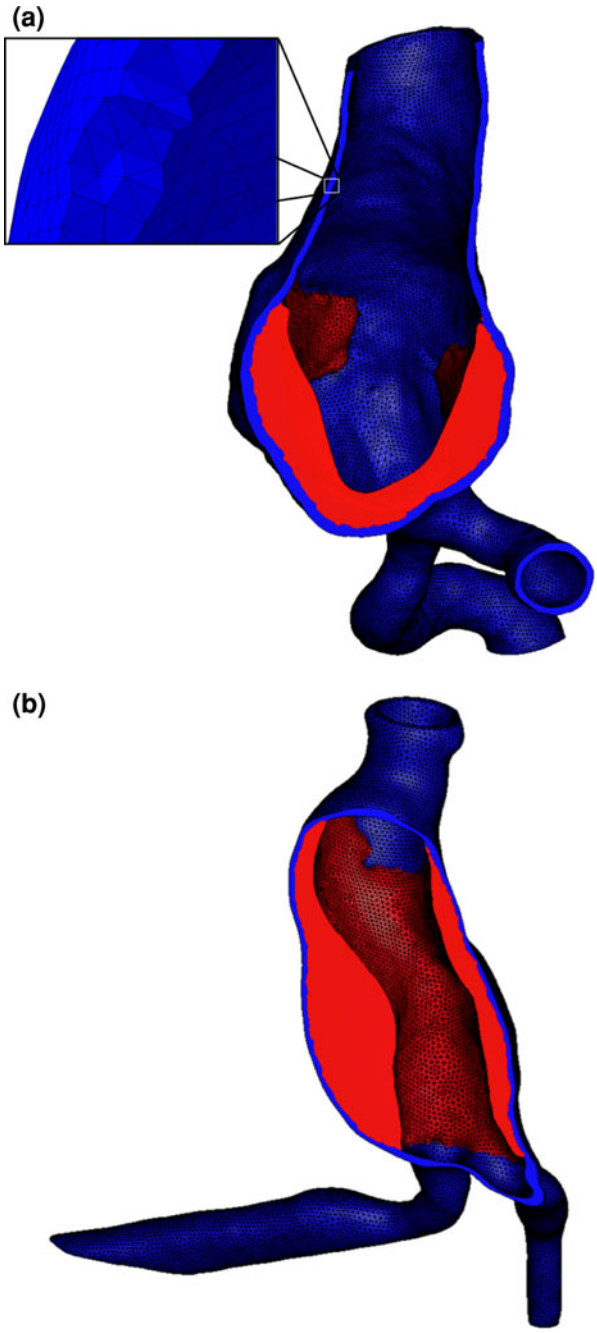

FIGURE 3. Finite element meshes of AAA geometries: (a) model A1 (inset shows a detail of the wall mesh) and (b) model A2.

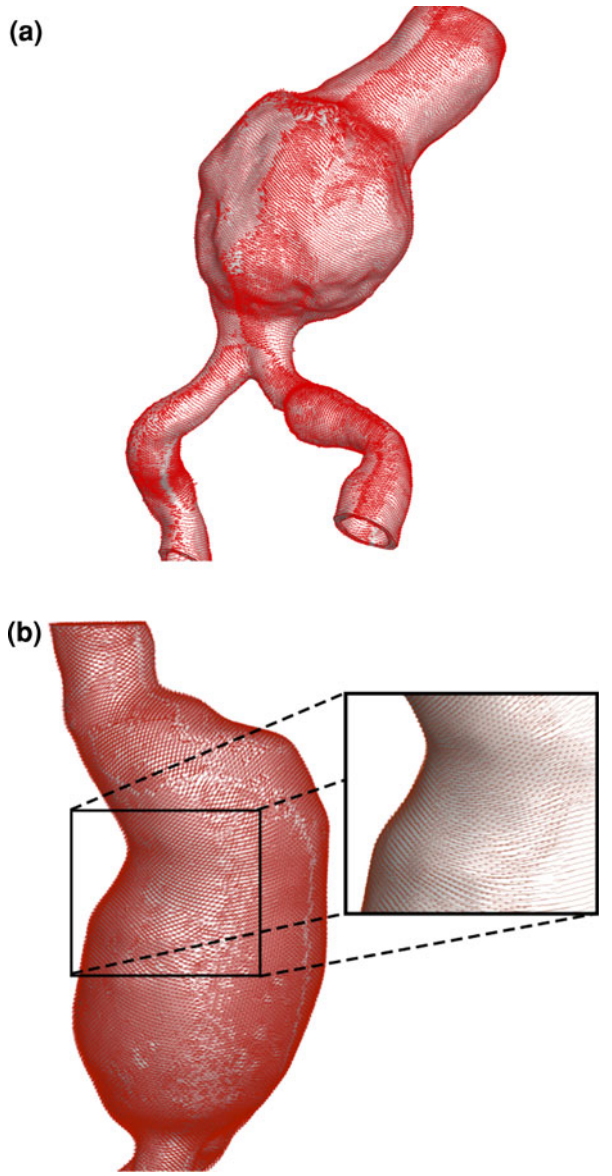

FIGURE 4. Circumferential direction of the AAA models: (a) model A1; (b) model A2. Circumferential directions were obtained according to the procedure proposed in Alastrue *et al.*[1]

Step ii When the elastic problem is solved, the kth zero-pressure geometry is computed by adding the difference $X^k_{\text{def}} - X_{\text{image}}$ to the $k-1$th zero-pressure geometry.
Step iii When using an anisotropic constitutive model ($f_{\text{aniso}} = 1$), the circumferential direction is pulled-back to the kth zero-pressure configuration, i.e., $n^k = \left(F^k\right)^{-1} n$ with the deformation gradient $F^k := \frac{\partial X_{\text{image}}}{\partial X^k_Z}$.
Step iv: The error norm is computed, and if it is less than *tol*, or the number of iterations is greater than the maximum allowed, $\max_{\text{iter}}$ the iteration is terminated.
Step v: The iterator k is incremented.

RESULTS

Validation

The algorithm was validated with an idealized cylindrical geometry. Because of the symmetry, only a

quarter of the cylinder was considered. The problem was set up such that its zero-pressure configuration corresponded to a cylinder of 20 cm length, an external diameter of 8 cm, and a uniform wall thickness of 0.5 cm. A quarter of the cylinder was discretized with 15,700 linear tetrahedral elements, and the arterial wall was assumed to be anisotropic with the circumferential direction being stiffer. Specifically, the SEF of Eq. (6) and material properties given in Table 1 were used for the computation. The pressurized geometry, X_{image}, was then obtained by inflating the cylinder at a pressure of 10.6 kPa (80 mmHg). Figure 6 shows the pressurized and the zero-pressure geometries. The algorithm's tolerance was set to 0.003 cm, i.e., less than a 0.1% relative difference between the actual and calculated zero-pressure geometries. The algorithm requires five iterations to reach the desired tolerance (see Fig. 7). Noteworthy is that the algorithm converged remarkably fast; after the second iteration the error is less than a 0.15%.

TABLE 3. Predicted peak PWS for model A2.

NE	PWS (kPa)	ΔPWS (%)
149,949	260	–
300,845	305	14.8
446,726	300	−1.7
815,588	310	3.2

Results for different meshes are shown, where NE denotes the number of elements. Change in PWS, ΔPWS, is computed between two consecutive mesh densities.

AAA Models

The algorithm described in "Zero-Pressure Geometry Algorithm" section was executed with a tolerance error of 0.2 mm (less than the image resolution). The

Given: X_{image}, circumferential direction (n), tol, $\max_{\text{iter}}$, f_{aniso}

Initialize: $k := 1$, $X_{\text{Z}}^0 := X_{\text{image}}$

Repeat

i) Find X_{def}^k from:

$$\nabla \cdot \sigma = 0 \text{ in } B^{k-1}$$

$$\sigma = 2\frac{1}{J}F\frac{\partial W}{\partial C}F^T$$

$$u\,|_{\partial B_t^{k-1}, \partial B_b^{k-1}} = \bar{u}$$

$$(\sigma \cdot m_i)\,|_{\partial B_i^{k-1}} = P_{\text{diast}}$$

ii) Update zero-pressure geometry

$$X_{\text{Z}}^k := X_{\text{Z}}^{k-1} + (X_{\text{def}}^k - X_{\text{image}})$$

iii) Fiber pull-back

if $f_{\text{aniso}} == 1$ then

$$F^k := \frac{\partial X_{\text{image}}}{\partial X_{\text{Z}}^k}$$

$$n^k := (F^k)^{-1} n$$

end if

iv) Error

$$error = \|X_{\text{def}}^k - X_{\text{image}}\|_\infty$$

v) $k := k + 1$

Until $(error \le tol$ and $k < \max_{\text{iter}})$

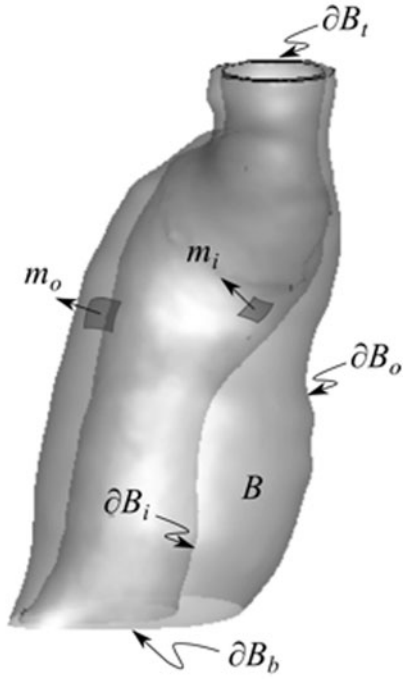

FIGURE 5. Zero-pressure geometry algorithm. The algorithm continuously updates the reference configuration of the AAA until the difference between the original CT-image and the deformed configuration obtained from the current zero-pressure geometry, X_{def}^k, is less than a prescribed tolerance, *tol*.

zero-pressure geometry for the 12 patient-specific AAA geometries was computed with isotropic and anisotropic material models. The difference between the CT-based geometry and the computed zero-pressure geometry for model A2 is shown in Fig. 8. Isotropic and anisotropic material models predicted almost the same zero-pressure configuration. The maximum displacement between CT-based and the computed zero-pressure geometries was about 14% and 16% for the isotropic and anisotropic model, respectively. For all models together the maximum difference between CT-based and zero-pressure geometries was 5.25 ± 1.21 and 5.35 ± 1.11 mm for the isotropic and anisotropic material models, respectively.

The computed PWS was 332 ± 160 and 357 ± 167 kPa for the isotropic and anisotropic material models, respectively, based on the zero-pressure geometry. These stresses are well in the range of failure stress reported in the literature. See for example by Raghavan *et al.*[30] (336–2,351 kPa with a median of 1266 kPa for ruptured and non-ruptured aneurysms), or Di Martino *et al.*[9] (820 ± 90 kPa for electively repaired aneurysms). However, the fact that we are using linear tetrahedral may prevent the prediction of accurate enough through the thickness stress gradient. It is important to mention that For model A1, the stress field obtained with the CT-based and the zero-pressure reference geometries is shown in Fig. 9. For the anisotropic wall model the predicted PWS was 630 kPa and 810 kPa for CT-based and the zero-pressure reference geometries, respectively. Hence, PWS increased approximately by 28% when considering the zero-pressure geometry. Results for the isotropic model are very similar. However, it is noted that the anisotropic model leads to slightly higher stresses. For model A1 the location of the maximum principal stress was found at the bulge within a thrombus-free region of the arterial wall (see Figs. 9c and 9d).

In all analyzed cases, PWS using the CT-based geometry was lower than PWS obtained with the zero pressure geometry, regardless of the material model used (see Fig. 10). Specifically, for isotropic and anisotropic models PWS was underestimated by 21% (SD 17%) and 14% (SD 14%), respectively. The difference between the predicted PWS for the CT-based and the zero-pressure geometry for both material models was tested with a paired, two-sided signed rank test. This test found that computations based on the zero-pressure geometry will predict a larger PWS than based on the CT-based geometry with larger probability ($p = 0.005$ for both isotropic and anisotropic material models). In addition, the difference between the predicted PWS based on the zero-pressure geometry for the isotopic and anisotropic material models of the wall was also tested for significance. In this case, no statistical difference was found ($p = 0.093$).

Figure 11 shows the PWS as a function of the maximum AAA diameter. These results used the anisotropic material model and considered the zero-pressure geometry as their reference and stress-free configuration. Although PWS somehow increases with the diameter, no clear correlation between both variables is seen ($\rho = 0.15$, $p = 0.64$). Specifically, the highest PWS is seen in model A1 that has a diameter of 5.1 cm, whereas for B2, with the largest diameter, PWS was lowest. Figure 12 shows the cross-sections at which PWS was predicted. In order to focus the iliac arteries are hidden the image.

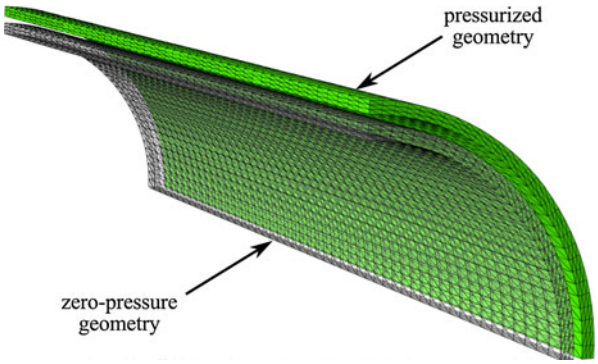

FIGURE 6. Idealized geometry used to validate the algorithm to compute the zero-pressure geometry. The cylinder in green corresponds to the pressurized geometry used as input information to compute the zero-pressure geometry. The wireframe corresponds to the zero-pressure geometry identified by the algorithm.

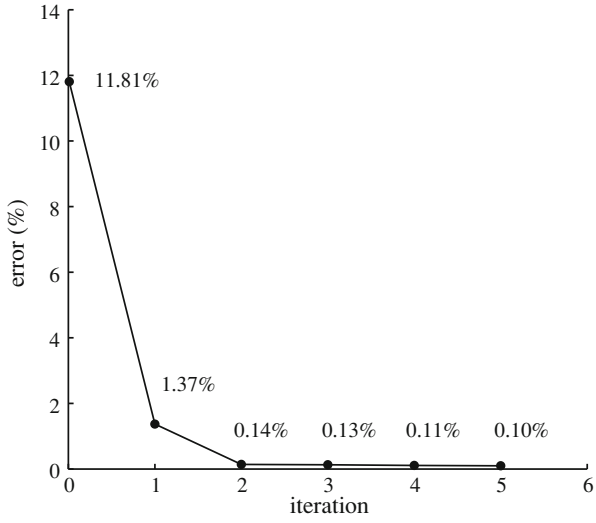

FIGURE 7. Convergence plot for the idealized geometry. The algorithm takes five iterations to reach the required tolerance (0.1%). Already, after the second iteration the error is less than 0.2%.

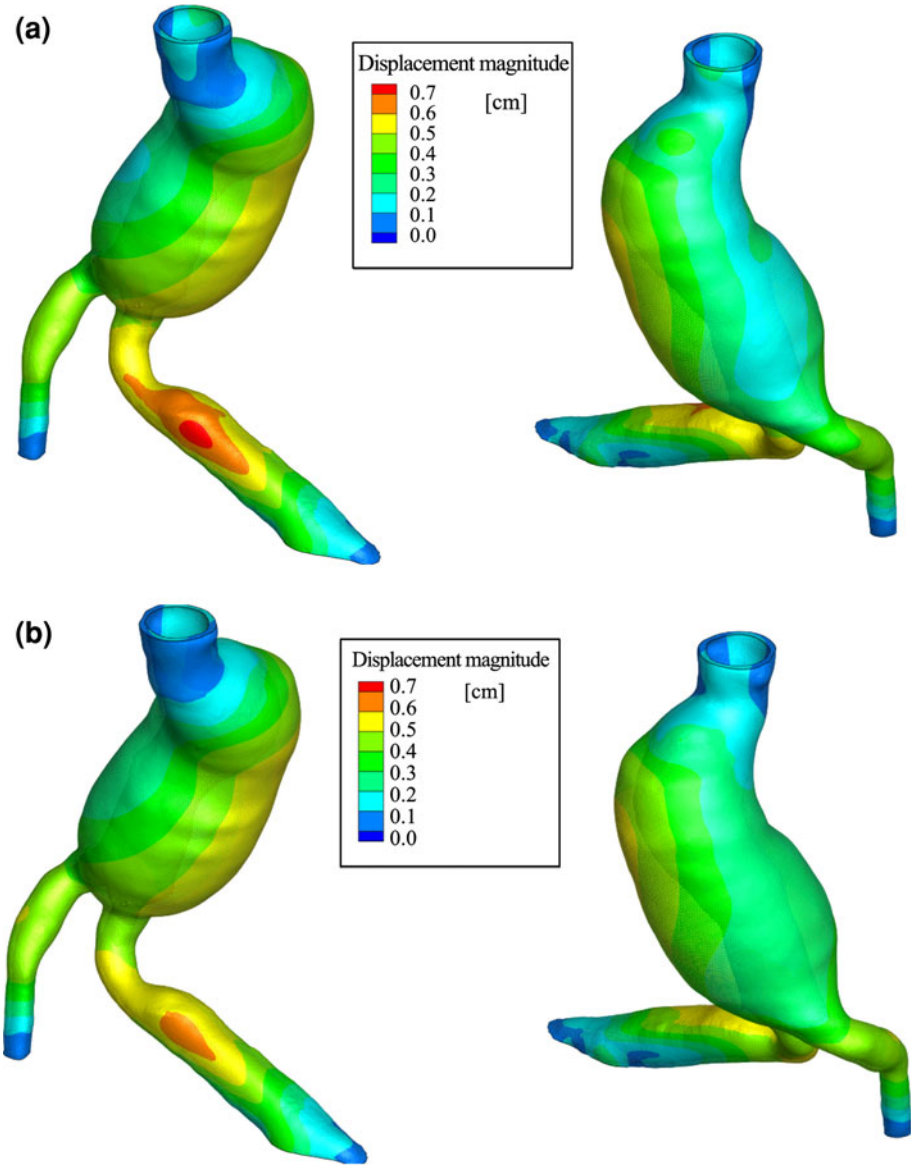

FIGURE 8. Difference between the zero-pressure and CT-based geometries (in cm) for aneurysm A2: (a) isotropic material model and (b) anisotropic material model.

Finally it is reported that the algorithm required between 5 and 13 iterations (on average 8 iterations) to find the zero-pressure geometry with a tolerated error of less than 0.2 mm. Figure 13 shows the convergence of the algorithm for aneurysm model A2, where isotropic and anisotropic wall models were considered. Note that after 4 iterations the error norm is already below the resolution of the CT images. The iterative procedure was also found to be globally volume preserving. Table 4 shows the percentage difference between the volumes of the final zero pressure and the CT-based geometries for models A1 and A2; the observed changes are negligible.

DISCUSSION

The importance to determine the AAA zero-pressure configuration is indicated by a number of publications in the past few years, and that it is generally accepted that PWS estimations that use the CT-based geometries can lead to errors.[6,24,29,40] Previously reported approaches assumed an isotropic wall and neglected the presence of ILT. This over-simplifies the biomechanical problem and questions the reliability of stress predictions. In addition, only few of the proposed methodologies consider the three-dimensional solid AAA wall.[6,40] The present work introduced a

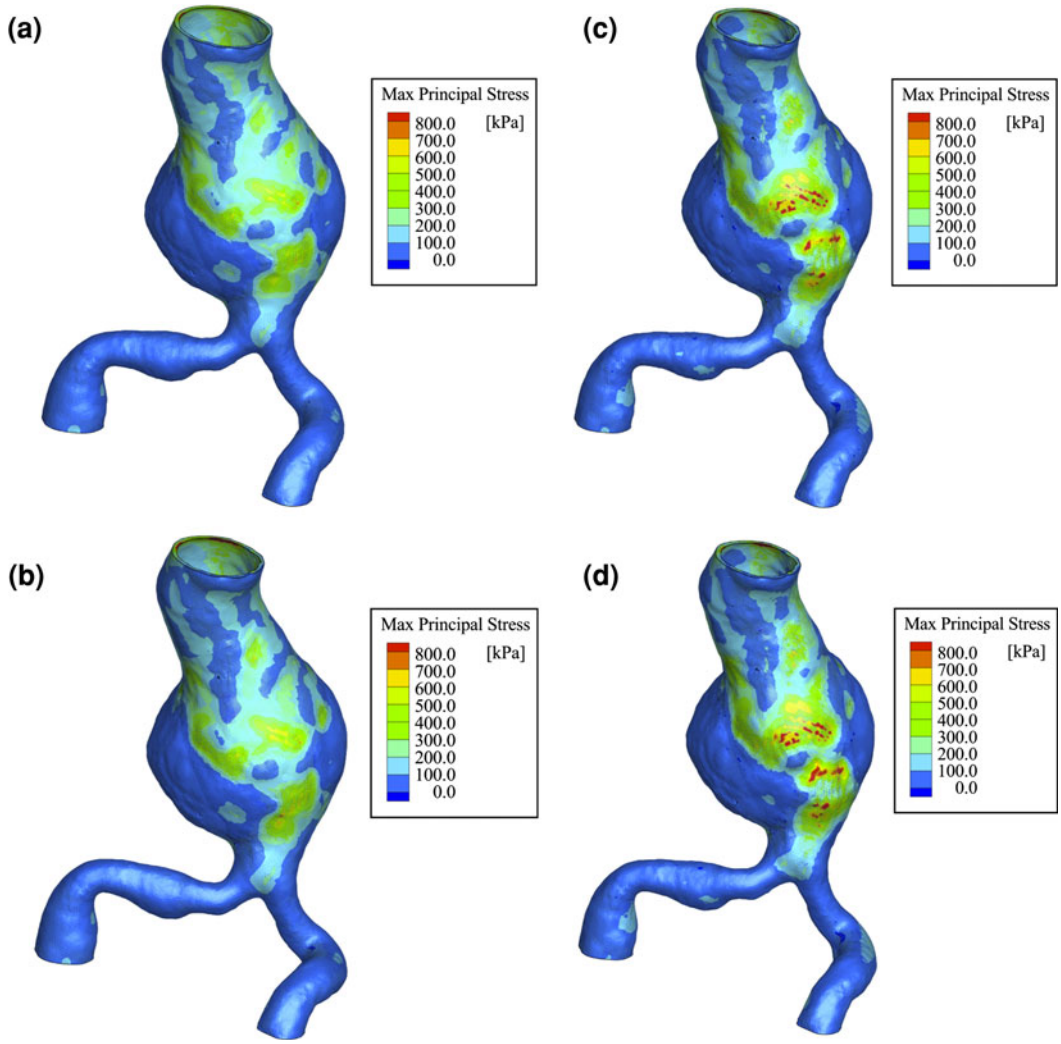

FIGURE 9. Maximum principal stress for model A1 (in kPa). (a) Isotropic model based on the CT-based geometry; (b) Anisotropic model based on the CT-based geometry; (c) Isotropic model based on the zero-pressure geometry; and (d) Anisotropic model based on the zero-pressure geometry.

novel methodology to predict the zero-pressure geometry of patient-specific AAAs and overcomes the above mentioned limitations. In contrast to approaches that consider the CT-based geometry as the reference configuration,[6,40] the present algorithm continuously updates the AAA reference configuration. Therefore, after convergence, the reference configuration corresponds to the zero-pressure geometry of the AAA. This has noticeable numerical advantages over the previously reported methodologies based on incremental upgrading of the deformation gradient.[6,40] Specifically, much larger increments can be used to find the zero-pressure. This is because in the present methodology, loading always starts from a zero-load reference configuration, instead of a loaded reference configuration as in the case of methodologies based on upgrading the deformation gradient.[6,40] When starting from a loaded configuration, the configuration is supposed to be in equilibrium with the applied pressure. Therefore, the inner pressure has to be incremented slowly as the deformation gradient is updated in order to avoid ill conditioning of the tangent matrix during the finite element analysis. This restriction implies a significantly larger number of iterations to converge to the zero-pressure geometry of the AAA. The algorithm presented in this work is a modification of the method proposed by Raghavan *et al.*,[29] which consists in finding a scaling factor, k, such that the zero pressure geometry can be obtained approximately as $X_z := X_{\text{image}} - kU$, where U is the normalized displacement field obtained by applying the diastolic pressure to the CT-based geometry. However, the methodology proposed by Raghavan *et al.* can only give approximate solutions as for any patient-specific

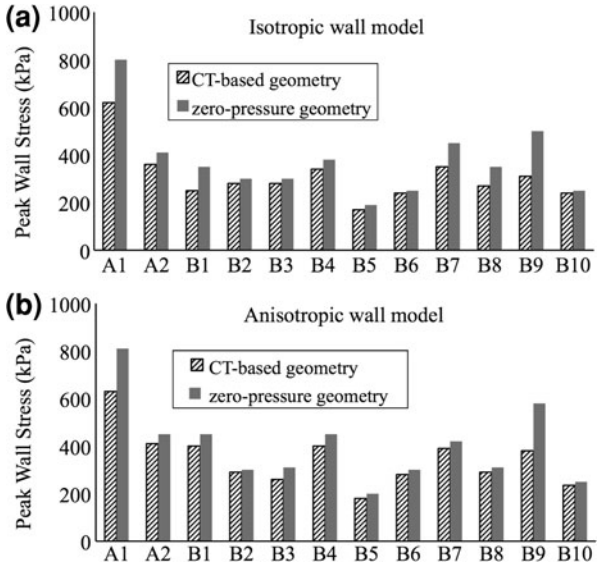

FIGURE 10. Predicted peak principal stresses in the AAA wall. Results use the CT-based (striped bars) and the zero-pressure (gray bars) geometries for their stress-free reference configurations. Predictions are based on an isotropic (a) and anisotropic (b) constitutive descriptions of the AAA wall.

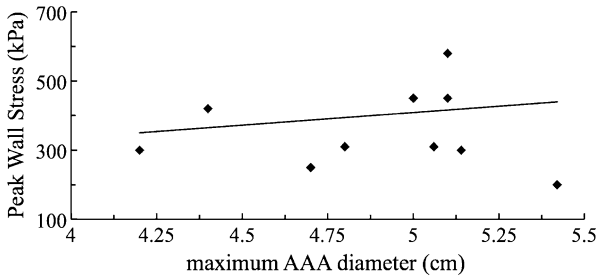

FIGURE 11. Peak principal stresses in the wall compared to the diameter of AAAs Predictions considered an anisotropic constitutive model for the AAA wall and the zero-pressure geometry as their stress-free reference configuration. The trend line shows a slight increase in the PWS with the maximum AAA diameter.

AAA it cannot be guaranteed that the vector **U** will be the same for any pressure increment applied to the model due to material and geometric nonlinearities.

Our simulation showed that in all 12 patient-specific geometries the proposed algorithm found the zero-pressure geometry in less than 13 iterations with a tolerated absolute error of 0.2 mm (or 1% relative error). Even more remarkably, setting the accuracy to the resolution of CT images (<0.7 mm), the algorithm identified in all cases the zero-pressure geometry in less than five iterations. Our results also showed that the proposed algorithm preserved the tissue volume globally, i.e., the zero-pressure and CT-based geometries had the same volume. This feature is particularly important for three-dimensional solid simulations of cardiovascular tissue, since the arterial wall and ILT are typically considered incompressible. This algorithmic feature is the direct consequence of using quasi-incompressible material descriptions (for the wall and the ILT) to predict the zero-pressure geometry. However, this kinematic restriction cannot be guaranteed at element level (Gauss points), as we observed local volume changes greater than 50%. It is important to point out that the proposed methodology is not absent of numerical problems due to distortion of the mesh during the iterative process. To mitigate this type of numerical problems, we make use of nearly isotropic meshes with a very regular distribution of element size. Using this approach we have found a good performance in all analyzed AAA geometries.

In this work, the material behavior had little influence on identifying the zero-pressure geometry (see Fig. 8). Specifically, the zero-pressure geometries obtained from isotropic and anisotropic material models differed by less than 3%. Similarly, PWS predictions were rather insensitive to the choice of the AAA wall model (see Figs. 9 and 10). This observation is partly caused by the biaxial stress–strain data reported in Vande Geest *et al.*,[44] which reflects an almost isotropic response of the AAA wall (see Fig. 1). Consequently, the models (5) and (6) were able to fit the data quite well with the anisotropic model outperforming the isotropic one slightly ($R^2 = 0.94$ for the isotropic material vs. $R^2 = 0.95$ for the anisotropic model). We used such a phenomenological approach to model the constitution of the aortic wall, although recently the collagen fiber distribution has been reported.[14] According to these data, an orthotropic collagen orientation distribution should be considered in a histological model. However, at least at a macroscopic length-scale, considering the detailed collagen organization might not have significant advantages over our approach.

The most remarkable changes in stress predictions were observed when changing between the CT-based and the zero-pressure geometries for the stress-free reference configuration of our simulations. Specifically, PWS obtained with the CT-based geometry was statistically significant lower than those obtained with the zero-pressure geometry. This observation hold for isotropic and anisotropic materials and was in agreement[6,40] as well as in disagreement[24] with previous reports. It is noted that previous conclusions have been derived without considering the ILT. Our results also point to the importance of considering ILT in biomechanical AAA simulations. The stress fields shown in Figs. 9 and 12 indicate that, in addition to AAA morphology and local wall curvature,[25,38] the ILT plays an important role in the biomechanical AAA rupture risk assessment. Similar conclusions were

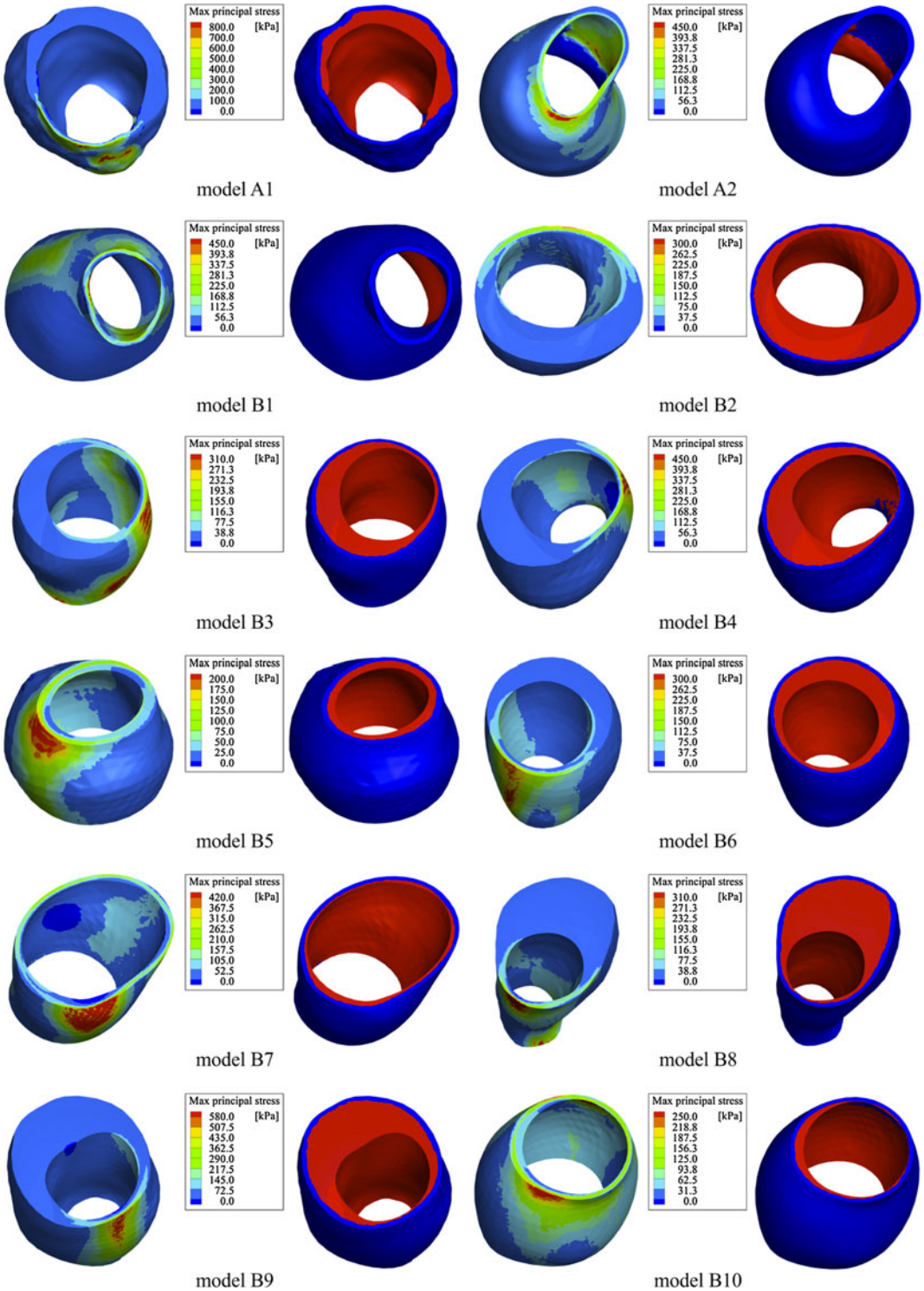

FIGURE 12. Cross-sections, where the PWS was predicted. Color-coded principal stresses plot (left) and segmented tissues with the ILT in red and the arterial wall in blue (right) are shown. Predictions considered an anisotropic constitutive model for the AAA wall and the zero-pressure geometry as their stress-free reference configuration.

reported from a retrospective study that compared ruptured and non-ruptured cases.[13]

Unfortunately, we did not have access to patient-specific intraluminal blood pressure and used instead mean diastolic and systolic arterial pressures of 80 mmHg (10.6 kPa) and 120 mmHg (16.0 kPa), respectively, for all our cases. Using patient-specific pressure data would have directly influenced the

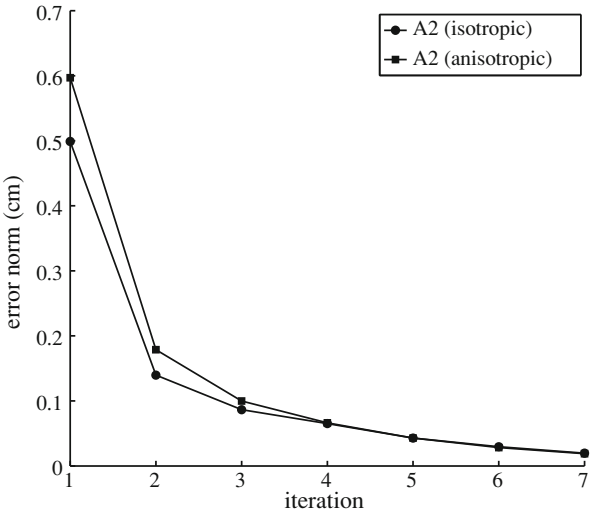

FIGURE 13. Convergence of the algorithm to predict the AAA zero-pressure geometry. Model A2 is considered and the computation used isotropic (circles) and anisotropic (squares) constitutive models for the AAA wall.

TABLE 4. Percentage volume change between the zero pressure and CT-based geometries.

	AAA A1		AAA A2	
	Isotropic (%)	Anisotropic (%)	Isotropic (%)	Anisotropic (%)
Percentage volume change	0.02	0.04	−0.008	−0.029

predicted wall stress, but would not have changed our conclusions regarding the importance of using the zero-pressure geometry in stress predictions. Finally, it is also noted that our computations did not consider residual stresses (and strains) in the zero-pressure configuration. Although well documented for healthy tissue, to the authors' knowledge there are no adequate experimental data available for AAA residual stresses.

CONCLUSION AND FUTURE WORK

A methodology was proposed to predict the zero-pressure geometry of aneurysms that is suitable for general three-dimensional solid models. Specifically, it allows for isotropic and anisotropic AAA wall models and considers the ILT. The proposed iterative method is stable and predicts the zero-pressure geometry with few iteration steps. However, since the methodology is based on finite element models, the quality of the initial mesh is vital for the performance of the algorithm.

Our results indicate a statistically significant influence of the zero-pressure geometry on the PWS as compared to predicted PWS based on the CT-based geometry. However, the choice of the material model is not as important since we did not find statistically significant differences in the predicted PWS based on the zero-pressure geometry with either material model for the AAA wall. The modeling of 12 patient-specific AAA geometries indicates that there must be other structural characteristics in the geometry that have an influence on the PWS. It is noted that in most cases the PWS was located at the bare arterial wall of the bulge that was not covered by the ILT. These results suggest that the geometrical configuration of the ILT relative to the arterial wall may be an influential factor not only on the ensuing peak wall stress, but also on its location within the lesion. This observation is in agreement with Wang *et al.*[47] which reports that the modeling of ILT to the 3D stress analysis AAA has a profound influence on the magnitude and distribution of wall stresses.

Finally, although we have only considered AAAs in this work, the algorithm can be applied to a variety of biological structures under pressure, e.g., the heart, atria, and brain aneurysms among others. The results achieved with our algorithm underscores the important effect of using the zero-pressure geometry to compute PWS values, which is also in agreement with previous studies.

ACKNOWLEDGMENTS

The authors would like to acknowledge research funding from project 071/UPB10/12 from the University of Zaragoza, and from NIH grants R21EB007651, R21EB008804 and R15HL087268. The content is solely the responsibility of the authors and does not necessarily represent the official views of the National Institutes of Health.

REFERENCES

[1]Alastrué, V., A. García, E. Peña, J. F. Rodríguez, M. Martínez, and M. Doblaré. Numerical framework for patient-specific computational modelling of vascular tissue. *Commun. Numer. Methods Eng.* 6:1–30, 2006.

[2]Auer, M., and T. C. Gasser. Reconstruction and finite element mesh generation of abdominal aortic aneurysms from computerized tomography angiography data with minimal user interactions. *IEEE Trans. Med. Imaging* 29(4):1022–1028, 2010.

[3]Brown, L. C., and J. L. Powell. Risk factors for aneurysm rupture in patients kept under ultrasound surveillance. UK small aneurysm trial participants. *Ann. Surg.* 230(3):289–296, 1999; discussion 296–297.

[4]Carlson, D. E. Inverse deformation results for elastic materials. *Z. Angew. Math. Phys.* 20(2):261–263, 1969.
[5]Chadwick, P. Application of an energy-momentum tensor in elastostatics. *J. Elasticity* 5:249–258, 1975.
[6]de Putter, S., B. J. B. M. Wolters, M. C. M. Ruttena, M. Breeuwer, F. A. Gerritsen, and F. N. van de Vosse. Patient-specific initial wall stress in abdominal aortic aneurysms with a backward incremental method. *J. Biomech.* 40:1081–1090, 2006.
[7]Demiray, H. A note on the elasticity of soft biological tissues. *J. Biomech.* 5:309–311, 1972.
[8]Di Martino, E. S., and D. A. Vorp. Effect of variation in intraluminal thrombus constitutive properties on abdominal aortic aneurysm wall stress. *Ann. Biomed. Eng.* 31(7):804–809, 2003.
[9]DiMartino, E. S., A. Bohra, J. P. Vande Geest, N. Y. Gupta, M. S. Makaroun, and D. A. Vorp. Biomechanical properties of ruptured versus electively repaired abdominal aortic aneurysm wall tissue. *J. Vasc. Surg.* 43:570–576, 2006.
[10]Fillinger, M. F., S. P. Marra, M. L. Raghavan, and F. E. Kennedy. Prediction of rupture risk in abdominal aortic aneurysm during observation: wall stress versus diameter. *J. Vasc. Surg.* 37(4):724–732, 2003.
[11]Fillinger, M. F., M. L. Raghavan, S. P. Marra, J. L. Cronenwett, and F. E. Kennedy. In vivo analysis of mechanical wall stress and abdominal aortic aneurysm rupture risk. *J. Vasc. Surg.* 36(3):589–597, 2002.
[12]Gasser, T. C. Bringing vascular biomechanics into clinical practice. Simulation-based decisions for elective abdominal aortic aneurysms repair. In: Patient-Specific Computational Modeling. Lecture Notes in Computational Vision and Biomechanics, edited by B. Calvo, and E. Pena. Dordrecht: Springer, 2012.
[13]Gasser, T. C., M. Auer, F. Labruto, J. Swedenborg, and J. Roy. Biomechanical rupture risk assessment of abdominal aortic aneurysms: model complexity versus predictability of finite element simulations. *Eur. J. Vasc. Endovasc.* 40:176–185, 2010.
[14]Gasser, T. C., S. Gallinetti, X. Xing, C. Forsell, J. Swedenborg, and J. Roy. Spatial orientation of collagen fibers in the Abdominal Aortic Aneurysm's wall and its relation to wall mechanics. *Acta Biomater.* 8(8):3091–3103, 2012.
[15]Govindjee, S., and P. Mihalic. Computational methods for inverse finite elastostatics. *Comput. Methods Appl. Mech.* 136:47–57, 1996.
[16]Govindjee, S., and P. Mihalic. Computational methods for inverse deformations in quasi-incompressible finite elasticity. *Int. J. Numer. Methods Eng.* 43:821–838, 1998.
[17]Hans, S. S., O. Jareunpoon, B. Balasubramaniam, and G. B. Zelenock. Size and location of thrombus in intact and ruptured abdominal aortic aneurysms. *J. Vasc. Surg.* 41:584–588, 2005.
[18]Heng, M. S., M. J. Fagan, W. Collier, G. Desai, P. T. McCollum, and I. C. Chetter. Peak wall stress measurement in elective and acute abdominal aortic aneurysms. *J. Vasc. Surg.* 47:17–22, 2008.
[19]Holzapfel, G. A. Nonlinear Solid Mechanics. A Continuum Approach for Engineering. Chichester: John Wiley & Sons Ltd., 2000, 455 pp.
[20]Karkos, C., U. Mukhopadhyay, I. Papakostas, J. Ghosh, G. Thomson, and R. Hughes. Abdominal aortic aneurysm: the role of clinical examination and opportunistic detection. *Eur. J. Vasc. Endovasc. Surg.* 19:299–303, 2000.
[21]Kazi, M., J. Thyberg, P. Religa, J. Roy, P. Eriksson, U. Hedin, and J. Swedenborg. Influence of intraluminal thrombus on structural and cellular composition of abdominal aortic aneurysm wall. *J. Vasc. Surg.* 38(6):1283–1292, 2003.
[22]Larsson, E., F. Labruto, T. C. Gasser, J. Swedenborg, and R. Hultgren. Analysis of aortic wall stress and rupture risk in patients with abdominal aortic aneurysm with a gender perspective. *J. Vasc. Surg.* 54(2):295–299, 2011.
[23]Limet, R., N. Sakalihassan, and A. Albert. Determination of the expansion rate and incidence of rupture of abdominal aortic aneurysms. *J. Vasc. Surg.* 14(4):540–548, 1991.
[24]Lu, J., X. Zhou, and M. L. Raghavan. Inverse elastostatic stress analysis in pre-deformed biological structures: demonstration using abdominal aortic aneurysms. *J. Biomech.* 40:693–696, 2007.
[25]Maier, A., M. W. Gee, C. Reeps, J. Pongratz, H. H. Eckstein, and W. A. Wall. A comparison of diameter, wall stress, and rupture potential index for abdominal aortic aneurysm rupture risk prediction. *Ann. Biomed. Eng.* 38:3124–3134, 2010.
[26]Martufi, G., E. S. Di Martino, C. H. Amon, S. C. Muluk, and E. A. Finol. Three-dimensional geometrical characterization of abdominal aortic aneurysms: image-based wall thickness distribution. *ASME J. Biomech.* 131(6):061015, 2009.
[27]Newman, A. B., A. M. Arnold, G. L. Burke, D. H. O'Leary, and T. A. Manolio. Cardiovascular disease and mortality in older adults with small abdominal aortic aneurysms detected by ultrasonography: the cardiovascular health study. *Ann. Intern. Med.* 134(3):182–190, 2001.
[28]Powell, J. T., L. C. Brown, J. F. Forbes, F. G. Fowkes, R. M. Greenhalgh, C. V. Ruckley, and S. G. Thompson. Final 12-year follow-up of surgery versus surveillance in the UK Small Aneurysm Trial. *Br. J. Surg.* 94:702–708, 2007.
[29]Raghavan, M. L., M. A. Baoshun, and M. F. Filinger. Non-invasive determination of zero-pressure geometry of arterial aneurysms. *Ann. Biomed. Eng.* 34(9):1414–1419, 2006.
[30]Raghavan, M. L., J. Kratzberg, E. M. Castro de Tolosa, M. M. Hanaoka, P. Walker, and E. S. da Silva. Regional distribution of wall thickness and failure properties of human abdominal aortic aneurysm. *J. Biomech.* 39:3010–3016, 2006.
[31]Raghavan, M. L., and D. A. Vorp. Toward a biomechanical tool to evaluate rupture potential of abdominal aortic aneurysm: identification of a finite strain constitutive model and evaluation of its applicability. *J. Biomech.* 33(4):475–482, 2000.
[32]Rissland, P., Y. Alemu, J. Ricotta, and D. Blustein. Abdominal aortic aneurysm risk of rupture: patient-specific FSI simulations using anisotropic model. *ASME J. Biomech.* 131(3):031001, 2009.
[33]Rodriguez, J. F., G. Martufi, M. Doblare, and E. A. Finol. The effect of material model formulation in the stress analysis of abdominal aortic aneurysms. *Ann. Biomed. Eng.* 37(11):2218–2221, 2009.
[34]Rodriguez, J. F., C. Ruiz, M. Doblaré, and G. Holzapfel. Mechanical stresses in abdominal aortic aneurysms: influence of diameter, asymmetry, and material anisotropy. *ASME J. Biomech.* 130(2):021023, 2008.
[35]Sakalihasan, N., R. Limet, and O. D. Defawe. Abdominal aortic aneurysm. *Lancet* 365:1577–1589, 2005.
[36]Shield, R. T. Inverse deformation results in finite elasticity. *Z. Angew. Math. Phys.* 78:490–500, 1967.

[37]Shum, J., E. S. Di Martino, A. Goldhammer, D. Goldman, L. Acker, G. Patel, J. H. Ng, G. Martufi, and E. A. Finol. Semi-automatic vessel wall detection and quantification of wall thickness in computed tomography images of human abdominal aortic aneurysms. *Med. Phys.* 37(2):638–648, 2010.

[38]Shum, J., G. Martufi, E. S. Di Martino, C. B. Washington, J. Grisafi, S. C. Muluk, and E. A. Finol. Quantitative assessment of abdominal aortic aneurysm geometry. *Ann. Biomed. Eng.* 39(1):277–286, 2011.

[39]Shum, J., A. Xu, I. Chatnuntawech, and E. A. Finol. A Framework for the Automatic Generation of Surface Topologies for Abdominal Aortic Aneurysm Models. *Ann. Biomed. Eng.* 39(1):249–259, 2011.

[40]Speelman, L., E. M. Bosboom, G. W. Schurink, J. Buth, M. Breeuwer, M. J. Jacobs, and F. N. van de Vosse. Initial stress and nonlinear material behavior in patient-specific AAA wall stress analysis. *J. Biomech.* 42(11):1713–1719, 2009.

[41]Thompson, S. G., H. A. Ashton, L. Gao, R. A. P. Scott, and Multicentre Aneurysm Screening Study Group. Screening men for abdominal aortic aneurysm: 10 year mortality and cost effectiveness results from the randomised Multicentre Aneurysm Screening Study. *Brit. Med. J.* 338:2307, 2009.

[42]Thubrikar, M. J., J. al-Soudi, and F. Robicsek. Wall stress studies of abdominal aortic aneurysm in a clinical model. *Ann. Vasc. Surg.* 15(3):355–366, 2001.

[43]Truijers, M., J. A. Pol, L. J. Schultzekool, S. M. van Sterkenburg, M. F. Fillinger, and J. D. Blankensteijn. Wall stress analysis in small asymptomatic, symptomatic and ruptured abdominal aortic aneurysms. *Eur. J. Vasc. Endovasc. Surg.* 33(4):401–407, 2007.

[44]Vande Geest, J. P., M. S. Sacks, and D. A. Vorp. The effects of aneurysm on the biaxial mechanical behavior of human abdominal aorta. *J. Biomech.* 39(7):1324–1334, 2006.

[45]Venkatasubramaniam, A. K., M. J. Fagan, T. Mehta, K. J. Mylankal, B. Ray, G. Kuhan, I. C. Chetter, and P. T. McCollum. A comparative study of aortic wall stress using finite element analysis for rupture and non-ruptured abdominal aortic aneurysms. *Eur. J. Vasc. Endovasc. Surg.* 28:168–176, 2004.

[46]Vorp, D. A., M. L. Raghavan, and M. W. Webster. Wall stress studies of abdominal aortic aneurysms: influence of diameter, and asymmetry. *J. Vasc. Surg.* 27:632–639, 1998.

[47]Wang, D. H. J., M. S. Makaroun, M. W. Webster, and D. A. Vorp. Effect of intraluminal thrombus on wall stress in patient-specific models of abdominal aortic aneurysm. *J. Vasc. Surg.* 36:598–604, 2002.